Structural Basis of the Allosteric Inhibition of Human ABCG2 by Nanobodies

Rossitza N. Irobalieva [1], **Ioannis Manolaridis** [1], **Scott M. Jackson** [1], **Dongchun Ni** [2,3], **Els Pardon** [4,5], **Henning Stahlberg** [2,3], **Jan Steyaert** [4,5] and **Kaspar P. Locher** [1]*

1 - *Institute of Molecular Biology and Biophysics,* ETH Zürich, Otto-Stern-Weg 5, 8093 Zürich, Switzerland

2 - *Laboratory of Biological Electron Microscopy (LBEM),* Institute of Physics, School of Basic Science, École Polytechnique Fédérale de Lausanne (EPFL), Lausanne, Switzerland

3 - *Dept. of Fund. Microbiology,* Faculty of Biology and Medicine, University of Lausanne, Lausanne, Switzerland

4 - *Structural Biology Brussels,* Vrije Universiteit Brussel, VUB, Brussels, Belgium

5 - *VIB-VUB Center for Structural Biology,* VIB, Brussels, Belgium

Correspondence to Kaspar P. Locher: locher@mol.biol.ethz.ch *(K.P. Locher)* @lab_locher 🐦 *(K.P. Locher)*
https://doi.org/10.1016/j.jmb.2023.168234
Edited by Heather Pinkett

Abstract

ABCG2 is an ATP-binding cassette transporter that exports a wide range of xenobiotic compounds and has been recognized as a contributing factor for multidrug resistance in cancer cells. Substrate and inhibitor interactions with ABCG2 have been extensively studied and small molecule inhibitors have been developed that prevent the export of anticancer drugs from tumor cells. Here, we explore the potential for inhibitors that target sites other than the substrate binding pocket of ABCG2. We developed novel nanobodies against ABCG2 and used functional analyses to select three inhibitory nanobodies (Nb8, Nb17 and Nb96) for structural studies by single particle cryo-electron microscopy. Our results showed that these nanobodies allosterically bind to different regions of the nucleotide binding domains. Two copies of Nb8 bind to the apex of the NBDs preventing them from fully closing. Nb17 binds near the two-fold axis of the transporter and interacts with both NBDs. Nb96 binds to the side of the NBD and immobilizes a region connected to key motifs involved in ATP binding and hydrolysis. All three nanobodies prevent the transporter from undergoing conformational changes required for substrate transport. These findings advance our understanding of the molecular basis of modulation of ABCG2 by external binders, which may contribute to the development of a new generation of inhibitors. Furthermore, this is the first example of modulation of human multidrug resistance transporters by nanobodies.

Introduction

ABCG2, also known as the breast cancer resistance protein (BCRP)[1]; is an ATP-binding cassette (ABC) transporter expressed in the plasma membrane of cells of various tissues and tissue barriers.[2] ABCG2 is a multidrug transporter with a broad spectrum of substrates.[1,3,4] Together with other multidrug transporters, including ABCB1 and ABCC1, ABCG2 is overexpressed in certain types of cancer cells[5,6] and may contribute to multidrug resistance (MDR)[7–11] by reducing the accumulation of chemotherapeutic drugs in cancer cells (reviewed in[12–14]) ABC transporters have a substrate binding pocket formed by their transmembrane domains (TMDs) and conserved ATP binding sites between two cytoplasmic nucleotide-binding domains (NBDs). The binding and hydrolysis of

ATP powers substrate transport by inducing conformational changes in the TMDs (from inward-facing to outward-facing) - a process known as the "alternating access mechanism".[15] Over the past decades, significant effort has been made to develop small molecule inhibitors targeting the substrate binding pocket of MDR ABC transporters and to characterize the structural basis of their inhibitory activity.[16–19] However, clinical application of small-molecule inhibitors has not been successful due to either lack of specificity, high toxicity or poor oral availability.[20] Besides targeting the substrate-binding pocket, ABC transporter activity can also be inhibited by using the inorganic phosphate analog vanadate, which traps ADP at the catalytic site.[21–24] This approach is not useful for therapeutic applications given the large number of molecular machines that depend on ATP for their function. Therefore, new approaches are needed that allow specific inhibition of MDR ABC transporters without irreversibly blocking their binding pockets or ATP-binding sites.[25] Another mechanism to inhibit ABC transporters is by binding structural surface epitopes and interfering with essential conformational changes. One such example is the antigen-binding fragment of the inhibitory conformational antibody 5D3 (5D3-Fab),[26] which "clamps" the extracellular loops of ABCG2, trapping an "inward-open" conformation and preventing substrate release.[27] Prior to this study, there were no known cytoplasmic binders for ABCG2. We hypothesized nanobodies might be able to allosterically inhibit ABCG2. Nanobodies are single-domain variable fragments of camelid-derived heavy-chain antibodies. Their small size (13–14 kDa), stability and solubility make them potentially interesting agents for therapeutic applications, such as cancer diagnosis and therapy.[28,29] Inhibitory nanobodies have already been identified for bacterial ABC transporters, including the lipid-linked oligosaccharide flippase PglK and the vitamin B12 transporter BtuF.[30,31] Here, we generated nanobodies against human ABCG2, investigated their functional properties *in vitro*, and determined high-resolution structures by electron cryo-microscopy (cryo-EM) to explain how they bind to ABCG2 and exert their inhibitory function.

Results and Discussion

Generation and screening of nanobodies

To generate conformation-specific nanobodies, human ABCG2 was reconstituted into liposomes and injected into a llama (Figure 1(A)). To ensure that the resulting nanobodies recognize a physiologically relevant conformation of the transporter, no inhibitors or inhibitory proteins were present in the proteoliposome mixture. The nanobody generation yielded a pool of $\sim$50 nanobodies that bound to ABCG2, the majority of which reduced ATPase activity. Seven were selected for further studies – the three most inhibitory of the set and four that had a moderate impact on function. We further assessed the functional effect of this subset on liposome-reconstituted ABCG2 by measuring both the ATPase rate and the transport in the presence of radiolabeled estrone-3-sulfate (E_1S). The three most inhibitory nanobodies (here denoted as Nb8, Nb17 and Nb96; Figure S9) reduced the ATPase rate to less than 25% of the basal rate (Figure 1(B)). Their effect on ABCG2-mediated E_1S transport was even more pronounced, as transport was almost abolished in the presence of one of these nanobodies (Figure 1(C)). We found that each of the three nanobodies (Nb8, Nb17 and Nb96) exhibited an inhibitory effect comparable to that of 5D3-Fab (Figure 1(D)). Remarkably, the combination of 5D3-Fab and either Nb8 or Nb17 resulted in an almost complete inhibition of ABCG2 – an effect similar to that observed for the small molecule inhibitor Ko143.[16] This suggests that the three nanobodies bind to epitopes on ABCG2 that do not overlap with the binding site of 5D3-Fab and may therefore provide an alternative mode of inhibition.

Cryo-EM structures of ABCG2-Nb complexes and inhibitory mechanism

For high resolution structure determination, we used 5D3-Fab to increase the overall size of the particles and to guide their alignment during data processing. We thus determined the structures of nanodisc-reconstituted ABCG2 in complex with 5D3-Fab and either Nb8, Nb17 or Nb96 (Figures S1, S2, S3) to an overall resolution of 3.04 Å, 3.20 Å and 3.49 Å, respectively. The cryo-EM maps revealed that all three nanobodies bind to the NBDs, albeit at different epitopes (Figure 2(A)). The ABCG2-Nb binding interface of all three complexes was sufficiently resolved to allow for unambiguous assignment of individual residues (Figures 2(B-D), S4(A-C). None of the nanobodies interact directly with the ATP-binding motif, but the mechanistic changes they induce are sufficient to lock the transporter in an inward-open state, thereby interfering with ATP hydrolysis and substrate transport. The binding modes of these nanobodies are discussed separately below. We have also analyzed the structural changes observed in the NBDs that might prevent ABCG2 from transitioning to the ATP-bound state.

Nb8 – Two copies of Nb8 bind, with a binding site at the apex of the NBDs (Figure 2(A)). A stretch of residues from ABCG2 (residues S302-F313), which was disordered in all previous ABCG2 structures is ordered and bound to a groove on the surface of Nb8 (Figures 2(B), S4(A, D)). Residues from an α-helix of the NBD (I329-L349) also interact with the nanobody (Figure 2(B)). To analyze how Nb8 might affect conformational changes of ABCG2, we superimposed the binding
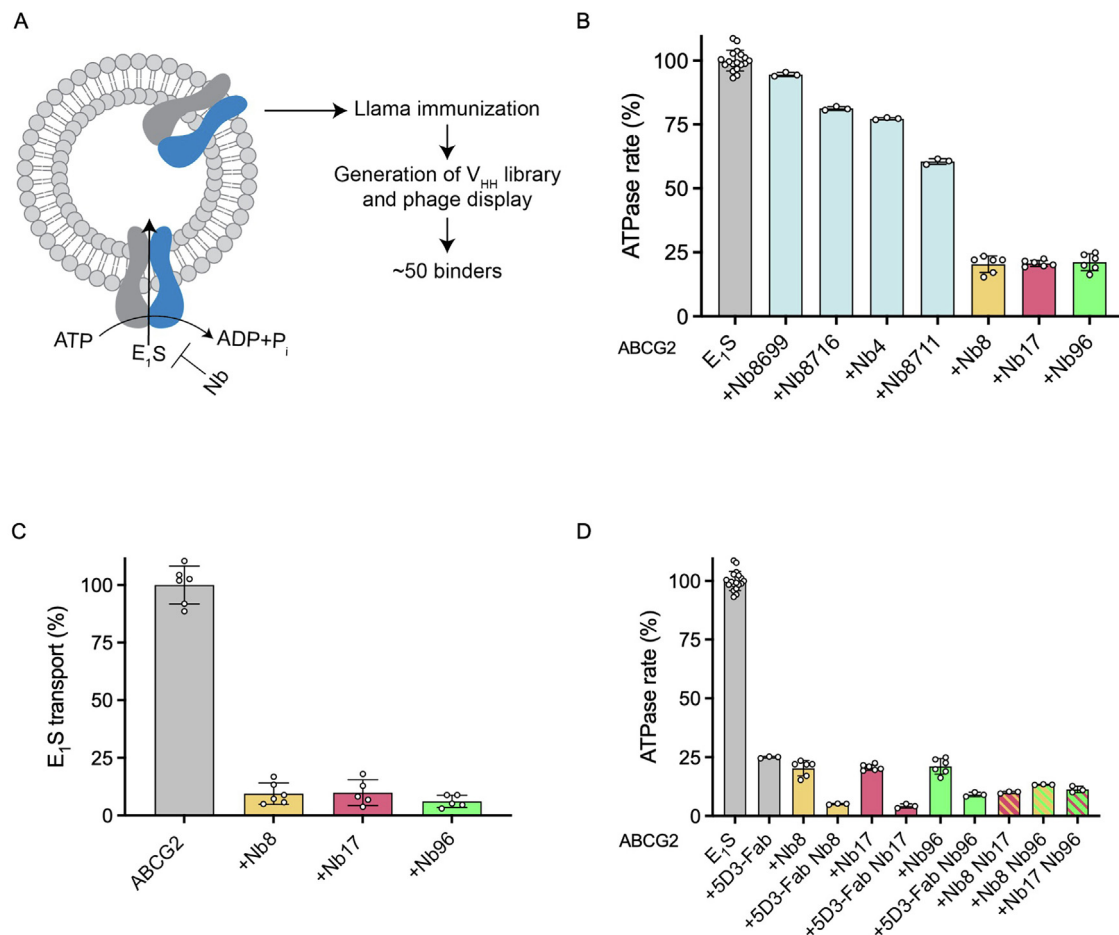
Figure 1. Functional modulation of human ABCG2 by nanobodies. A. Schematic representation of liposome reconstituted ABCG2 and nanobody generation. **B.** ATPase activity of liposome-reconstituted ABCG2 in the presence of E_1S and one of seven different nanobodies. **C.** Transport of E_1S by liposome-reconstituted ABCG2 in the presence of nanobodies. Bars show the mean initial E_1S transport activity; error bars show standard deviations; and dots show rates derived from each technical replicate (same batch of proteoliposomes). **D.** ATPase activity in the presence of E_1S, different nanobodies and 5D3-Fab. The bars show means, error bars show standard deviations and dots show rates derived from each technical replicate (same batch of proteoliposomes).

epitope of our ABCG2-Nb8 structure with the previously determined ATP-bound state (PDBID: **6HBU**) (Figures 3(A), S5(A)). In ATP-bound ABCG2, residues S302-E310 of one monomer participate in the formation of a short helix (Figure S6A, red color) that interacts with residues from the second monomer (not shown). We speculate that by stabilizing S302-F313, Nb8 prevents the formation of this helix and prevents the transport cycle from advancing to the next step.

Nb17 – Nb17 binds at the apex of the ABCG2 dimer near the twofold molecular and symmetry axis, where it interacts with both NBDs (Figures 2 (A,C), S4(B, D)). While the binding epitope of Nb17 partially overlaps with that of Nb8, its unique positioning makes it incompatible with the binding of a second copy of Nb17. Binding of Nb17 breaks the twofold symmetry of the NBDs of ABCG2. In one of the ABCG2 monomers, four residues

(S302-V305) from the disordered stretch discussed above are stabilized and ordered (Figures S6(B), black color). Superimposing the structure of the ATP-bound state on each monomer of Nb17-bound ABCG2 provides insight into the inhibitory mechanism (Figures 3(B) and S5(B)). Binding of Nb17 prevents the NBDs of ABCG2 from moving closer together, locking the transporter in an inward-open conformation, and preventing it from converting to the ATP-bound state.

Nb96 – The EM density map of the ABCG2-Nb96 complex showed clear density for a single Nb bound to the side of one NBD (Figure 2(A)). The corresponding site on the second NBD showed a weak, noisy density suggesting that for some transporters, it may be possible to bind two copies of Nb96. We focused on refining the subclass containing a single copy of Nb96 (Figure S3) and
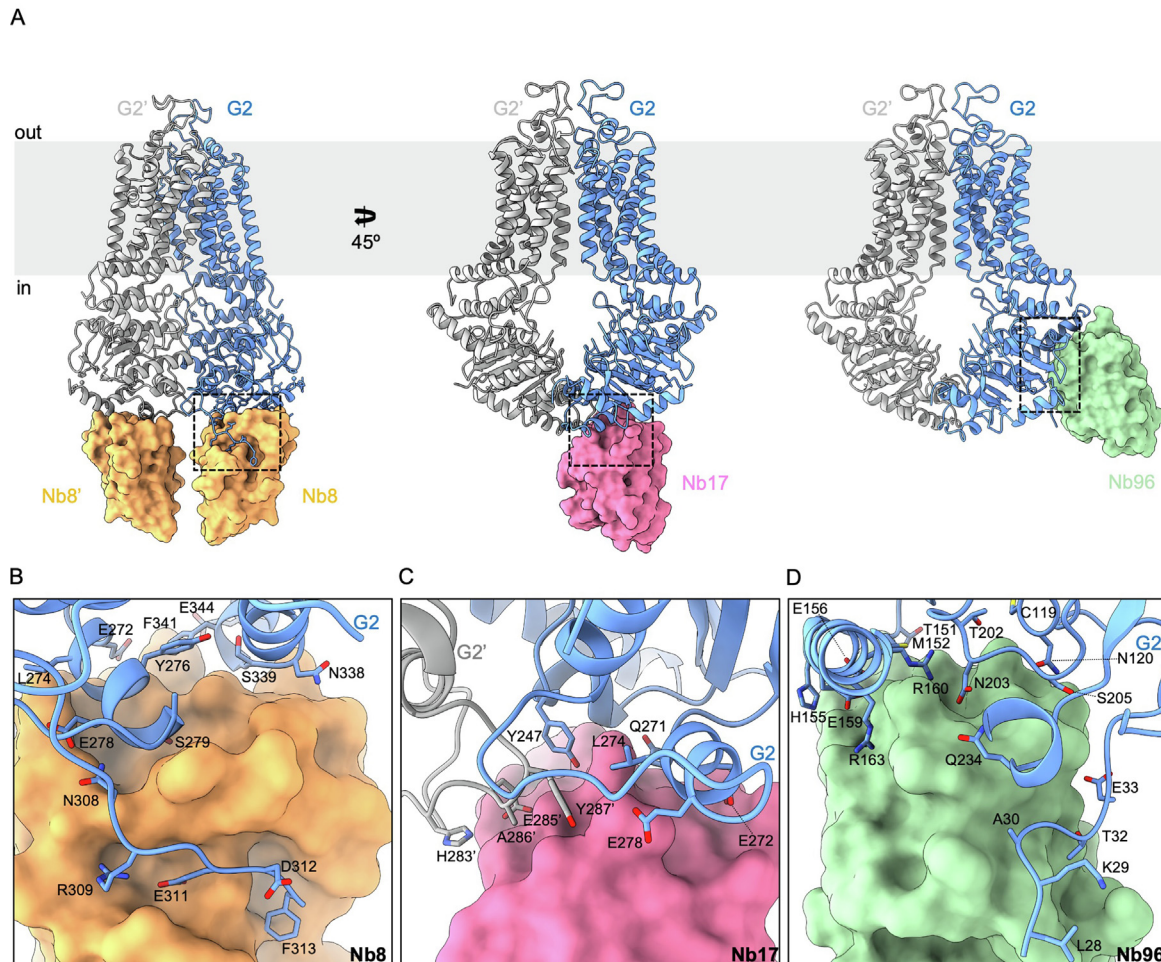
Figure 2. Structures of human ABCG2 with different nanobodies. Ribbon diagram of ABCG2 and surface representation for each nanobody. **A.** Overview of the structure of ABCG2 in a complex with Nb8 (left), Nb17 (middle) and Nb96 (right). The latter two are rotated 45° with respect to the first structure. ABCG2 subunits are colored in blue and gray. The prime symbol indicates residues of the gray-colored half transporter. Fab fragments used in this study, which bind the extracellular loops of the transporter, were omitted for clarity. Black rectangles indicate the interface between ABCG2 and each nanobody. Zoomed in views of the ABCG2-nanobody interface for all three complexes: ABCG2-Nb8 (**B**), ABCG2-Nb17 (**C**) and ABCG2-Nb96 **(D)**. Side chains of ABCG2 residues that interact with each nanobody (distance ≤ 3.5 Å) are shown as sticks and labelled. Color scheme and representation are same as in (**A**).

therefore applied C1 symmetry to the subsequent data processing steps. We observed that Nb96 stabilizes several otherwise disordered residues at the N-terminus of ABCG2 (L28-E33) (Figure 2(D), S4C, D), and the binding epitope also includes an α-helix formed by residues (N154-L168) and residues near the P-loop and the β-strand defining the Walker-B motif (Figures S7(A)). These key motifs in the NBD are known to drive ATP binding and hydrolysis. Superposition of residues T151-G169 of the NBD with the corresponding region of ATP-bound ABCG2 (PDBID: **6HBU**) revealed that when Nb96 is bound, a shift of the helix N154-L168 cannot occur, because it would cause a clash with nearby residues (Figures S6(C), red surface). The location of the Nb96 binding site restricts the motion of (at least one of) the NBDs

(Figure S7) and a single copy of Nb96 is sufficient to obstruct the function of the transporter.

In summary, binding of any of these three nanobodies is incompatible with ABCG2 adopting an ATP-bound, closed conformation (Figures 3, S5), thereby preventing substrate transport.

Comparison with other ABC transporters and their binders

Cytoplasmic binders, both inhibitory and non-inhibitory, have been reported for several ABC transporters (Figure S8). Since the NBDs of ABC transporters are highly conserved, we compared the binding epitopes of the three new nanobodies described here with those of other known allosteric binders specific for members of the G
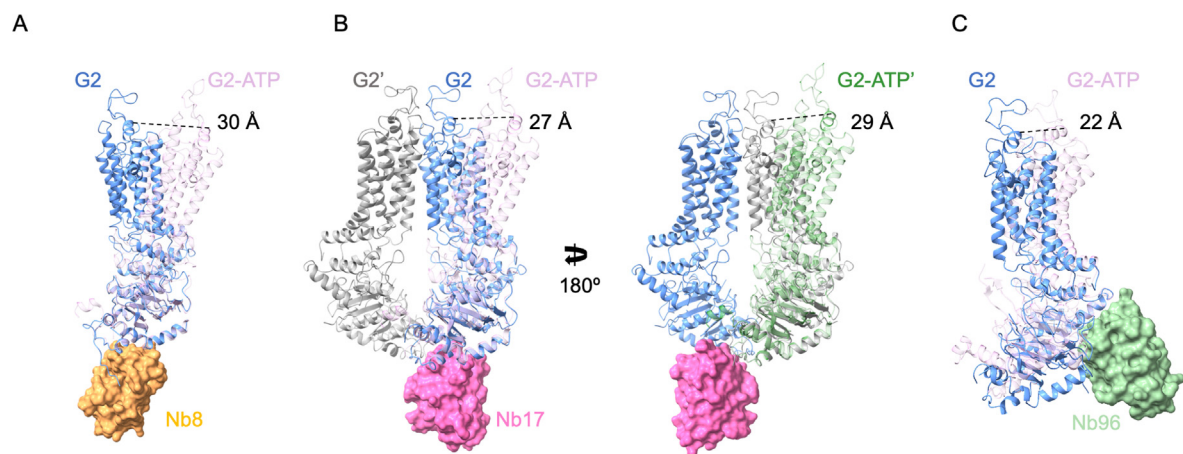
Figure 3. Structural basis of the inhibitory effect of nanobodies on human ABCG2. Monomers of Nb-bound ABCG2 are denoted with blue (G2) and gray (G2′). Nanobodies are colored orange (Nb8) (**A**), pink (Nb17) (**B**) or green (Nb96) (**C**) and shown as surfaces. G2-ATP denotes a single monomer of the ATP bound state of ABCG2 (PDBID: **6HBU**) and is shown in light pink (**A**, **B**) or green (**B**, **C**). The relative distance between the superimposed models is indicated.
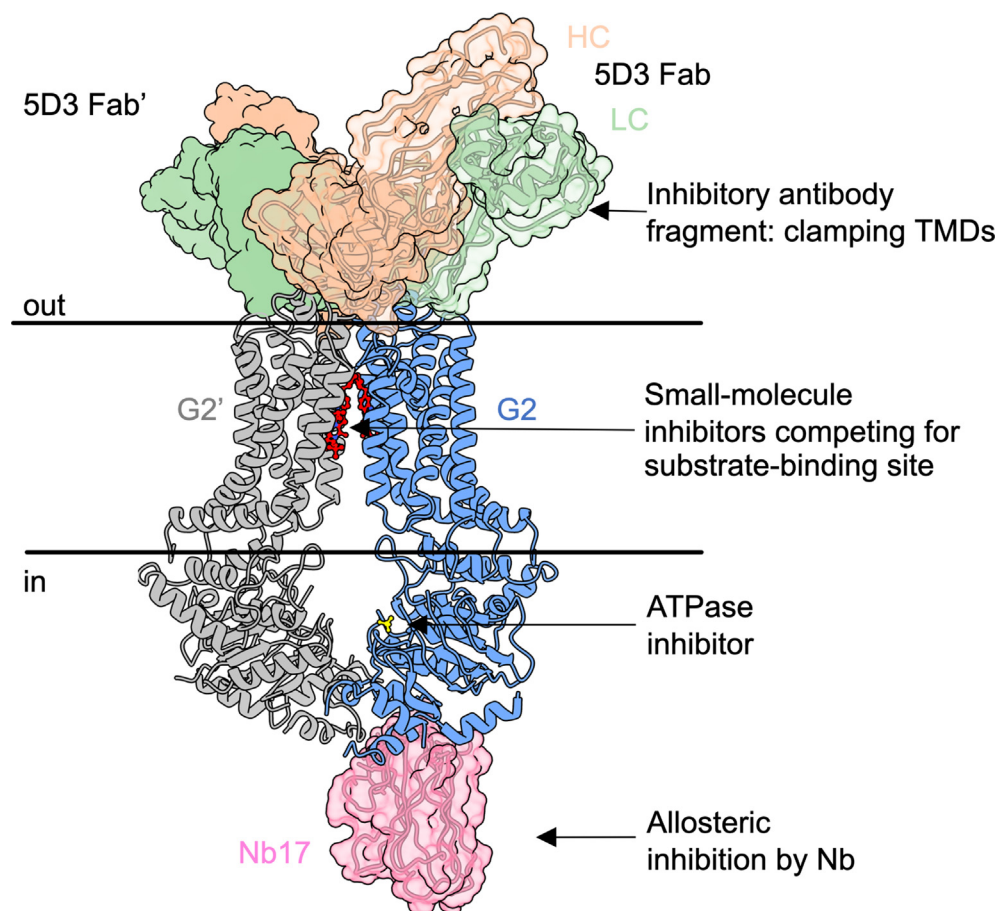

Figure 4. Distinct mechanisms of human ABCG2 inhibition. Ribbon diagram of the ABCG2 dimer (blue and gray) with different modes of inhibition shown simultaneously. Small molecule inhibitors (red) occupy the central substrate binding pocket. ATPase inhibitors, such as vanadate (yellow), occupy the ATP-binding site. Inhibitory binders, such as the antibody 5D3 Fab (orange/green surfaces and ribbon) and a nanobody (pink ribbon and surface) bind externally.

and B-subfamilies. One example we looked at is the heterodimeric cholesterol transporter ABCG5/G8, which shares a high sequence similarity with ABCG2. Three Fabs have been developed against ABCG5/G8 for structural studies. Two of them are inhibitory (Fab 2C7 and Fab 2E10) and one (Fab 11F4) stimulates the ATPase activity of ABCG5/G8.[32,33] The two inhibitory Fabs (Fab 2C7 and Fab 2E10) have overlapping epitopes of binding and are close to the binding site of the inhibitory Nb96 on ABCG2. Nb96 and Fab 2E10 interact with similar motifs in their respective NBD domains and we expect that they act similarly to limit the conformational changes required for ATP hydrolysis. Intriguingly, the binding epitope for the stimulatory Fab 11F4 on ABCG5/G8 is close to where the inhibitory Nb8 and Nb17 bind ABCG2. These observations suggest that it is difficult to predict the effect that cytoplasmic binders may have on the function of a transporter, despite having structurally similar epitopes.

Another example we considered is ABCB4, a transporter expressed in the canalicular membrane of hepatocytes and that translocates lipids into the bile canaliculi. Two distinct synthetic antibodies can simultaneously bind ABCB4 (Figure S8).[34] 4B1-Fab binds the elbow helix and the NBD-TMD interface, whereas QA2-Fab binds exclusively the NBD, similar to how Nb96 binds ABCG2. Unlike Nb96, neither of the ABCB4-specific Fabs is inhibitory. In contrast to the G-subfamily, the B-subfamily of transporters differ in the architecture of their TMDs. These differences affect the position of the NBDs relative to the membrane, with the NBDs of the B-subfamily positioned further away from the membrane compared to the G-subfamily. This could explain the different effect QA2-Fab and Nb96 have on the function of ABCB4 and ABCG2.

Conclusion

Several members of the ABC family of transporters, including ABCG2, have been identified as contributing factor in MDR. Understanding the precise mechanism of these transporters has been critical in developing strategies to inhibit their function. While Fabs and small molecules (both competitive and non-competitive[35]) have been described as potential inhibitors, the use of nanobodies had not been previously explored. Here, we developed inhibitory nanobodies that target binding epitopes on the cytosolic side of ABCG2 and exert their function by locking the NBDs in a conformation that is incompatible with ATP-hydrolysis. Our work adds to the list of approaches that can be used to inhibit the function of ABCG2 (Figure 4). A challenge in using cytoplasmic binders for therapeutic application is the need to deliver them intracellularly. Promising methods for intracellular delivery of nanobodies

include the use of adenoviral vectors[36] and *in vitro* transcribed mRNA.[37] While the discussion here focuses on the identification of inhibitory nanobodies for ABCG2, it is important to note that non-inhibitory nanobodies are equally interesting in that they may have an application in protein maturation studies, where one can track the transporter inside the cell and investigate transporter folding and dimerization. We envision that this type of modulation could be extended to other membrane transporters of interest.

Materials and Methods

Expression and purification of wild-type human ABCG2

Human ABCG2, containing an amino (N)-terminal Flag tag, was expressed in HEK293-EBNA (Thermo Fisher Scientific) cells, and purified as described previously.[16,27,38]

Expression and purification of 5D3-Fab

5D3 hybridoma cells, producing the 5D3 monoclonal antibody, were obtained from B. Sorrentino.[26] The cells were cultured in WHEATON CELLine Bioreactors, according to the manufacturer's protocol, and 5D3-Fab was then purified from the supernatant, as described in the Pierce Preparation Kit protocol (Thermo Fisher Scientific).

Expression and purification of nanobodies

Nanobodies were produced in the Steyaert laboratory, following established protocols,[39] and using as antigen liposome-reconstituted ABCG2 prepared as previously described.[27] Nanobodies were expressed and purified as previously described.[31,39] IMAC-purified and PD10-desalted nanobodies were assessed for purity and monodispersity by analytical size-exclusion chromatography (Superdex 75, gel filtration column), as well as SDS-PAGE, and finally concentrated and stored in buffer containing 50 mM Tris-HCl pH 7.5, 250 mM NaCl, 0.5 mM EDTA and 10% v/v glycerol. Nanobody naming convention in the manuscript corresponds to the following names in the Steyaert library: Nb8 (CA6348), Nb17 (CA6358), Nb96 (CA8696).

Nanodisc reconstitution of ABCG2

The membrane scaffold protein (MSP) 1D1 was expressed and purified and ABCG2 was reconstituted into brain polar lipid (BPL)/cholesterol hemisuccinate (CHS) nanodiscs as described previously.[16,27,38] To generate the ABCG2-Nb samples for cryo-EM studies, ABCG2 was first mixed with a threefold molar excess of 5D3-Fab and Nb before reconstitution.

ABCG2-liposome preparation

A BPL/cholesterol (BPL/chol) (Avanti Polar Lipids) mixture was prepared at a 4:1 (w/w) ratio as described previously.[16] Briefly, the BPL/chol mixture was extruded through a 400-nm polycarbonate filter and destabilized with 0.17% (v/v) Triton X100. Detergent-purified ABCG2 was then mixed with BPL/chol at a 100:1 (w/w) lipid/protein ratio. Detergent was removed with BioBeads, and proteoliposomes were spun at 100,000 g, resuspended in 25 mM HEPES, pH 7.5, 150 mM NaCl at a final lipid concentration of 10 mg ml^{-1}, and the reconstitution efficiency was determined.[40]

ATPase assays

ATP-hydrolysis activity was measured using a previously described technique.[41] ABCG2 proteoliposome were first freeze-thawed five times in the presence or absence of a three-fold molar excess of 5D3-Fab to ensure that 5D3-Fab was inside the proteoliposomes before extrusion.[16,27] The proteliposomes were then incubated with a 3-fold molar excess of each nanobody and 50 μM E$_1$S for 10 min at 37 °C prior to the addition of 2 mM ATP and 10 mM MgCl$_2$ to start the hydrolysis reaction. Data were recorded at four time intervals (0, 5, 15 and 30 min) and subsequent ATPase rates were determined using linear regression in GraphPad Prism 7.00. Rates were corrected for the orientation of ABCG2 in proteoliposomes.[27]

Transport assays

The transport of E$_1$S by liposome reconstituted ABCG2 was measured as previously described.[16,27,38] Proteoliposomes were extruded through a 400 nm polycarbonate filter and then incubated for 5 min at 30 °C in the presence of 5 mM MgCl$_2$, 50 μM ^{3}H-E$_1$S, and in the presence or absence of a 3-fold molar excess of nanobody. 25 mM Hepes pH 7.5/ 150 mM NaCl buffer was used. The transport reaction was initiated by the addition of 2 mM ATP. To stop the reaction, samples were removed, added to ice-cold stop buffer (25 mM HEPES, pH 7.5, 150 mM NaCl, 100 μM unlabelled E$_1$S). Samples were then filtered using a Multiscreen vacuum manifold (MSFBN6B filter plate, Millipore) and radioactivity trapped on the filters was measured using a Perkin Elmer 2450 Microbeta2 microplate scintillation counter. Initial transport rates from 30 s to 2 min were determined using linear regression in GraphPad Prism 7.00 and rates were corrected for the orientation of ABCG2 in proteoliposomes.[27]

Sample Preparation, Cryo-EM data acquisition and analysis

Formed complexes were purified using size exclusion chromatography and samples were applied to glow-discharged Quantifoil R1.2/1.3 carbon/copper 300 mesh grids and plunge-frozen in a liquid ethane/propane mixture with a Vitrobot Mark IV (FEI) with the chamber set to 4 °C and 100% humidity. An aliquot of 4 μl at a concentration of 1 mg/ml was applied onto each grid.

Data for ABCG2-5D3-Fab-Nb8 and ABCG2-5D3-Fab-Nb17 were collected at the ScopeM facility in ETH Zürich on a Titan Krios microscope, operated at 300 kV and equipped with a Gatan Quantum-LS energy filter (20 eV zero loss filtering) and a Gatan K2 Summit direct electron detector. Semi-automated data acquisition was performed with SerialEM.[42] Data were collected in super-resolution mode at a nominal magnification of 165,000x and pixel size of 0.42 Å/pixel. Image stacks contained 40 frames with a total dose of 72 e$^-$/A^2 for the ABCG2-5D3-Fab-Nb8 sample and 68 e$^-$/A^2 for the ABCG2_Nb17 sample. The defocus was in the range of −0.6 to −2.4 μm with a step size of 0.2 μm. Data collection for ABCG2_Nb8 was performed in two different sessions on the same microscope – 2296 movies and 5223 movies, respectively. The ABCG2-5D3-Fab-Nb17 data set comprised 2847 movies.

Data for ABCG2-5D3-Fab-Nb96 were collected at C-CINA at the University of Basel on a Titan Krios, operated at 300 kV, and equipped with a Gatan Quantum-LS energy filter (20 eV zero loss filtering), containing a K2 Summit direct electron detector. Images were recorded in counting mode at a nominal magnification of 165,000x with a pixel size of 0.82 Å/pixel. The defocus was in the range of −0.8 to −2.8 μm with a step size of 0.1 μm. Exposures were 9 s, dose-fractionated into 45 frames, resulting in a total dose of 72 e$^-$/A^2. A total of 9129 movies were collected over two sessions.

Details of the data processing are summarized in Figures S1-S3 and in Table S1. Movies for the ABCG2-5D3-Fab-Nb8 and ABCG2-5D3-Fab-Nb17 samples were imported into Relion 3.1[43] and motion-corrected with MotionCor2.[44] Motion corrected micrographs were binned by a factor of two to 0.84 Å/pix. Contrast Transfer Function (CTF) parameters were estimated using Gctf.[45] Initially, reference-free particle autopicking with Laplacian-of-Gaussian filtering was performed, followed by several rounds of 2D and 3D classification. Per-particle Bayesian polishing and CTF refinement were performed on the subset of particles that were used for the final refinement. Movies for ABCG2-5D3-Fab-Nb96 were motion corrected in MotionCor2 (22) and imported into cryoSPARC v.2[46] for CTF estimation with CTFFIND[47] and further processing. The resolution of the final EM density maps was estimated using the Fourier shell correlation (FSC) at the cutoff of 0.143.[48]

ABCG2-5D3-Fab-Nb8: The two independent data sets were processed separately up and including the 2D classification. After that, particles were joined and final round of 2D classification

was performed, which yielded 529,054 particles that were then subjected to 3D classification. *Ab initio* model (C1) was generated in Relion 3.1. The 3D classification yielded three classes, two of which were well defined. The particles from those two classes (424,915) were subjected to several rounds of 3D refinement, 3D classification without alignment, particle polishing and per-particle CTF refinement and a subsequent final refinement with C2 symmetry imposed, followed by post-processing (B-factor sharpening). We used a mask that excluded the density for the nanodisc and constant domain of the 5D3-Fab. The resolution of the final, post-processed EM density map was 3.0 Å and included 233,072 particles.

ABCG2-5D3-Fab-Nb17: After several rounds of 2D classification, 206,548 particles were subjected to two rounds of 3D classification. *Ab initio* model (C1) was generated in Relion 3.1. 3D classification yielded classes that did not have a strong density for Nb17, indicating that some of the particles did not have Nb17 bound. The rest of the particles (109,985) were subjected to further rounds of 3D refinement, particle polishing and per-particle CTF refinement. The final EM density map was post-processed (B-factor sharpened) and had an overall resolution of 3.2 Å. We again used a mask that excluded the density for the nanodisc and constant domain of the 5D3-Fab.

ABCG2-5D3-Fab-Nb96: Initially, particles were manually picked and the resulting 2D classes were used as a template for particle picking of all micrographs. After 2D classification, 646,251 particles were selected for further processing. Several rounds of multi-class 3D classification were performed, followed by the heterogenous refinement and non-uniform refinement routines in cryoSPARC v2.[46] We saw classes that suggested either one or two copies of Nb96 bound per transporter. The best resolved class showed strong density for only one Nb96 bound. Further refinement was focused on the particles (98,009) from that class with C1 symmetry imposed and followed by local refinement with a soft global mask. The overall resolution was estimated at 3.49 Å.

Model building, refinement and validation

Model building was carried out in Coot[49] using as an initial model and template a previously published structure of ABCG2 (PDB: **6ETI**) and the nanobody structure (PDB: **5OVW**, chain G). Both models were rigid body-fitted into the EM density, manually inspected and modified where necessary, with the nanobody CDR loops built *de novo.* Refinement of the atomic coordinates was performed in Phenix[50] and validation in MolProbity.[51] 3DFSC was calculated and histograms and directional FSC plots were generated on the online 3DFSC Processing Server.[52] Per-residue Q-scores were calculated for one ABCG2 monomer with Nb8 and the entire ABCG2-5D3-Fab-Nb17 and ABCG2-5D3-Fab-Nb96 complexes. The red line represents the expected Q-score per residue based on the reported overall resolution. Q-scores were calculated with the MapQ plug-in[53] in UCSF Chimera.[54]

Figure Preparation

Graph preparation and data analysis was performed in GraphPad Prism version 8.4.3 for Mac, GraphPad Software, San Diego, California USA, https://www.graphpad.com. The images of EM density maps and models were prepared in UCSF Chimera[54] and UCSF ChimeraX.[55,56] Sequence alignment was performed in Clustal Omega[57] and visualized in Jalview.[58]

Author Contributions

K.P.L, I.M and S.M.J designed the project and planned the experiments; I.M. expressed and purified ABCG2 and 5D3-Fab. S.M.J. reconstituted ABCG2 into liposomes and lipidic nanodiscs and performed transport and ATPase activity assays. I.M. and S.M.J. purified nanobodies. E.P. performed immunization and cloning of ABCG2-specific Nbs. J.S. supervised Nb production. I.M. prepared cryo-grids and collected cryo-EM data for ABCG2-Nb8 and ABCG2-Nb17. R.N.I. collected additional data for ABCG2-Nb8. I.M and R.N.I. processed cryo-EM data. D.N. collected and processed data for ABCG2-Nb96. I.M., R.N.I. and K.P.L. refined and validated the models. R.N.I. and K.P.L. wrote the manuscript with input from I.M, S.M.J, E.P, J.S., H.S and D.N.

CRediT authorship contribution statement

Rossitza N. Irobalieva: Investigation, Formal analysis, Visualization, Writing - original draft, Writing - review & editing. **Ioannis Manolaridis:** Conceptualization, Methodology, Investigation, Formal analysis, Writing – review & editing. **Scott M. Jackson:** Conceptualization, Methodology, Investigation, Formal analysis. **Dongchun Ni:** Investigation, Formal analysis, Visualization. **Els Pardon:** Investigation, Formal analysis, Resources. **Henning Stahlberg:** Resources, Supervision. **Jan Steyaert:** Resources, Supervision. **Kaspar P. Locher:** Conceptualization, Methodology, Formal analysis, Supervision, Project administration, Resources, Funding acquisition, Writing - original draft, Writing - review & editing.

DATA AVAILABILITY

Data will be made available on request.

DECLARATION OF COMPETING INTEREST

The authors declare that they have no known competing financial interests or personal relationships that could have appeared to influence the work reported in this paper.

Acknowledgements

Appendix A. Supplementary data

Supplementary data to this article can be found online at https://doi.org/10.1016/j.jmb.2023.168234.

References

1. Doyle, L.A., Yang, W., Abruzzo, L.V., Krogmann, T., Gao, Y., Rishi, A.K., et al., (1998). A multidrug resistance transporter from human MCF-7 breast cancer cells. *Proc. Natl. Acad. Sci.* **95**, 15665–15670.

2. Fetsch, P.A., Abati, A., Litman, T., Morisaki, K., Honjo, Y., Mittal, K., et al., (2006). Localization of the ABCG2 mitoxantrone resistance-associated protein in normal tissues. *Cancer Letter* **235**, 84–92.

3. Ross, D.D., Yang, W., Abruzzo, L.V., Dalton, W.S., Schneider, E., Lage, H., et al., (1999). Atypical multidrug resistance: breast cancer resistance protein messenger RNA expression in mitoxantrone-selected cell lines. *JNCI J. Natl. Cancer Inst.* **91**, 429–433.

4. Allikmets, R., Schriml, L.M., Hutchinson, A., Romano-Spica, V., Dean, M., (1998). A human placenta-specific ATP-binding cassette gene (ABCP) on chromosome 4q22 that is involved in multidrug resistance. *Cancer Res.* **58**, 5337–5339.

5. Ross, D.D., Karp, J.E., Chen, T.T., Doyle, L.A., (2000). Expression of breast cancer resistance protein in blast cells from patients with acute leukemia: Presented in part at the Fortieth Annual Meeting of the American Society of Hematology, Miami Beach, FL, December 4–8, 1998. *Blood* **96**, 365–368.

6. Diestra, J.E., Scheffer, G.L., Català, I., Maliepaard, M., Schellens, J.H., Scheper, R.J., et al., (2002). Frequent expression of the multi-drug resistance-associated protein BCRP/MXR/ABCP/ABCG2 in human tumours detected by the BXP-21 monoclonal antibody in paraffin-embedded material. *J. Pathol.* **198**, 213–219.

7. Grant, C.E., Valdimarsson, G., Hipfner, D.R., Almquist, K.C., Cole, S.P., Deeley, R.G., (1994). Overexpression of multidrug resistance-associated protein (MRP) increases resistance to natural product drugs. *Cancer Res.* **54**, 357–361.

8. Ueda, K., Cardarelli, C., Gottesman, M.M., Pastan, I., (1987). Expression of a full-length cDNA for the human "MDR1" gene confers resistance to colchicine, doxorubicin, and vinblastine. *Proc. Natl. Acad. Sci.* **84**, 3004–3008.

9. Bruhn, O., Cascorbi, I., (2014). Polymorphisms of the drug transporters ABCB1, ABCG2, ABCC2 and ABCC3 and their impact on drug bioavailability and clinical relevance. *Expert Opin. Drug Metab. Toxicol.* **10**, 1337–1354.

10. Cole, S.P.C., (2014). Targeting multidrug resistance protein 1 (MRP1, ABCC1): past, present, and future. *Annu. Rev. Pharmacol. Toxicol.* **54**, 95–117.

11. Cole, S.P.C., Bhardwaj, G., Gerlach, J.H., Mackie, J.E., Grant, C.E., Almquist, K.C., et al., (1992). Overexpression of a transporter gene in a multidrug-resistant human lung cancer cell line. *Science* **258**, 1650–1654.

12. Gottesman, M.M., Fojo, T., Bates, S.E., (2002). Multidrug resistance in cancer: role of ATP–dependent transporters. *Nature Rev. Cancer* **2**, 48–58.

13. Assaraf, Y.G., Brozovic, A., Gonçalves, A.C., Jurkovicova, D., Linē, A., Machuqueiro, M., et al., (2019). The multi-factorial nature of clinical multidrug resistance in cancer. *Drug Resist. Updat.* **46**, 100645

14. Krishnamurthy, P., Schuetz, J.D., (2006). Role of ABCG2/BCRP in biology and medicine. *Annu. Rev. Pharmacol. Toxicol.* **46**, 381–410.

15. Locher, K.P., (2016). Mechanistic diversity in ATP-binding cassette (ABC) transporters. *Nature Struct. Mol. Biol.* **23**, 487–493.

16. Jackson, S.M., Manolaridis, I., Kowal, J., Zechner, M., Taylor, N.M.I., Bause, M., et al., (2018). Structural basis of small-molecule inhibition of human multidrug transporter ABCG2. *Nature Struct. Mol. Biol.* **25**, 333–340.

17. Kowal, J., Ni, D., Jackson, S.M., Manolaridis, I., Stahlberg, H., Locher, K.P., (2021). Structural basis of drug recognition by the multidrug transporter ABCG2. *J. Mol. Biol.* **433**, 166980

18. Nosol, K., Romane, K., Irobalieva, R.N., Alam, A., Kowal, J., Fujita, N., et al., (2020). Cryo-EM structures reveal distinct mechanisms of inhibition of the human multidrug transporter ABCB1. *PNAS* **117**, 26245–26253.

19. Stefan, S.M., Wiese, M., (2019). Small-molecule inhibitors of multidrug resistance-associated protein 1 and related processes: a historic approach and recent advances. *Med. Res. Rev.* **39**, 176–264.

20. Weidner, L.D., Zoghbi, S.S., Lu, S., Shukla, S., Ambudkar, S.V., Pike, V.W., et al., (2015). The inhibitor Ko143 is not specific for ABCG2. *J. Pharmacol. Exp. Ther.* **354**, 384–393.

21. Urbatsch, I.L., Sankaran, B., Weber, J., Senior, A.E., (1995). P-glycoprotein is stably inhibited by vanadate-induced trapping of nucleotide at a single catalytic site. *J. Biol. Chem.* **270**, 19383–19390.

22. Taguchi, Y., Yoshida, A., Takada, Y., Komano, T., Ueda, K., (1997). Anti-cancer drugs and glutathione stimulate vanadate-induced trapping of nucleotide in multidrug resistance-associated protein (MRP). *FEBS Letter* **401**, 11–14.

23. Szabó, K., Szakács, G., Hegeds, T., Sarkadi, B., (1999). Nucleotide occlusion in the human cystic fibrosis transmembrane conductance regulator. Different patterns in the two nucleotide binding domains. *J. Biol. Chem.* **274**, 12209–12212.

24. Sharma, S., Davidson, A.L., (2000). Vanadate-induced trapping of nucleotides by purified maltose transport complex requires ATP hydrolysis. *J. Bacteriol.* **182**, 6570–6576.

25. Liu, F., Zhang, Z., Levit, A., Levring, J., Touhara, K.K., Shoichet, B.K., et al., (2019). Structural identification of a hotspot on CFTR for potentiation. *Science* **364**, 1184–1188.

26. Zhou, S., Schuetz, J.D., Bunting, K.D., Colapietro, A.-M., Sampath, J., Morris, J.J., et al., (2001). The ABC transporter Bcrp1/ABCG2 is expressed in a wide variety of stem cells and is a molecular determinant of the side-population phenotype. *Nature Med.* **7**, 1028–1034.

27. Taylor, N.M.I., Manolaridis, I., Jackson, S.M., Kowal, J., Stahlberg, H., Locher, K.P., (2017). Structure of the human multidrug transporter ABCG2. *Nature* **546**, 504–509.

28. Jovcevska, I., Muyldermans, S., (2020). The therapeutic potential of nanobodies. *BioDrugs* **34**, 11–26.

29. Verhaar, E.R., Woodham, A.W., Ploegh, H.L., (2021). Nanobodies in cancer. *Semin. Immunol.* **52**, 101425

30. Perez, C., Köhler, M., Janser, D., Pardon, E., Steyaert, J., Zenobi, R., et al., (2017). Structural basis of inhibition of lipid-linked oligosaccharide flippase PglK by a conformational nanobody. *Sci. Rep.* **7**, 46641.

31. Mireku, S.A., Sauer, M.M., Glockshuber, R., Locher, K.P., (2017). Structural basis of nanobody-mediated blocking of BtuF, the cognate substrate-binding protein of the Escherichia coli vitamin B12 transporter BtuCD. *Sci. Rep.* **7**, 14296.

32. Zhang, H., Huang, C.-S., Yu, X., Lee, J., Vaish, A., Chen, Q., et al., (2021). Cryo-EM structure of ABCG5/G8 in complex with modulating antibodies. *Communications Biology.* **4**, 526.

33. Sun, Y., Wang, J., Long, T., Qi, X., Donnelly, L., Elghobashi-Meinhardt, N., et al., (2021). Molecular basis of cholesterol efflux via ABCG subfamily transporters. *PNAS* **118**, e2110483118

34. Nosol, K., Bang-Sørensen, R., Irobalieva, R.N., Erramilli, S.K., Stieger, B., Kossiakoff, A.A., et al., (2021). Structures of ABCB4 provide insight into phosphatidylcholine translocation. *PNAS* **118**

35. Guragossian, N., Belhani, B., Moreno, A., Nunes, M.T., Gonzalez-Lobato, L., Marminon, C., et al., (2021). Uncompetitive nanomolar dimeric indenoindole inhibitors of the human breast cancer resistance pump ABCG2. *Eur. J. Med. Chem.* **211**, 113017

36. Silva-Pilipich, N., Smerdou, C., Vanrell, L., (2021). A small virus to deliver small antibodies: new targeted therapies based on AAV delivery of nanobodies. *Microorganisms* **9**, 1956.

37. Zhou, X., Hao, R., Chen, C., Su, Z., Zhao, L., Luo, Z., et al., (2020). Rapid delivery of nanobodies/VHHs into living cells via expressing in vitro-transcribed mRNA. *Mol. Ther. Methods Clin. Dev.* **17**, 401–408.

38. Manolaridis, I., Jackson, S.M., Taylor, N.M.I., Kowal, J., Stahlberg, H., Locher, K.P., (2018). Cryo-EM structures of a human ABCG2 mutant trapped in ATP-bound and substrate-bound states. *Nature* **563**, 426–430.

39. Pardon, E., Laeremans, T., Triest, S., Rasmussen, S.G., Wohlkönig, A., Ruf, A., et al., (2014). A general protocol for the generation of nanobodies for structural biology. *Nature Protoc.* **9**, 674–693.

40. Schaffner, W., Weissmann, C., (1973). A rapid, sensitive, and specific method for the determination of protein in dilute solution. *Anal. Biochem.* **56**, 502–514.

41. Chifflet, S., Torriglia, A., Chiesa, R., Tolosa, S., (1988). A method for the determination of inorganic phosphate in the presence of labile organic phosphate and high concentrations of protein: application to lens ATPases. *Anal. Biochem.* **168**, 1–4.

42. Mastronarde, D.N., (2005). Automated electron microscope tomography using robust prediction of specimen movements. *J. Struct. Biol.* **152**, 36–51.

43. Zivanov, J., Nakane, T., Forsberg, B.O., Kimanius, D., Hagen, W.J.H., Lindahl, E., et al., (2018). New tools for automated high-resolution cryo-EM structure determination in RELION-3. *Elife*, 7.

44. Zheng, S.Q., Palovcak, E., Armache, J.-P., Verba, K.A., Cheng, Y., Agard, D.A., (2017). MotionCor2: anisotropic correction of beam-induced motion for improved cryo-electron microscopy. *Nature Methods* **14**, 331–332.

45. Zhang, K., (2016). Gctf: Real-time CTF determination and correction. *J. Struct. Biol.* **193**, 1–12.

46. Punjani, A., Rubinstein, J.L., Fleet, D.J., Brubaker, M.A., (2017). cryoSPARC: algorithms for rapid unsupervised cryo-EM structure determination. *Nature Methods* **14**, 290–296.

47. Rohou, A., Grigorieff, N., (2015). CTFFIND4: fast and accurate defocus estimation from electron micrographs. *J. Struct. Biol.* **192**, 216–221.

48. Kucukelbir, A., Sigworth, F.J., Tagare, H.D., (2014). Quantifying the local resolution of cryo-EM density maps. *Nature Methods* **11**, 63–65.

49. Emsley, P., Lohkamp, B., Scott, W.G., Cowtan, K., (2010). Features and development ofCoot. *Acta Crystallogr. D Biol. Crystallogr.* **66**, 486–501.

50. Adams, P.D., Afonine, P.V., Bunkóczi, G., Chen, V.B., Davis, I.W., Echols, N., et al., (2010). PHENIX: a comprehensive Python-based system for macromolecular structure solution. *Acta Crystallogr. D Biol. Crystallogr.* **66**, 213–221.

51. Williams, C.J., Headd, J.J., Moriarty, N.W., Prisant, M.G., Videau, L.L., Deis, L.N., et al., (2018). MolProbity: more and better reference data for improved all-atom structure validation. *Protein Sci.* **27**, 293–315.

52. Tan, Y.Z., Baldwin, P.R., Davis, J.H., Williamson, J.R., Potter, C.S., Carragher, B., et al., (2017). Addressing preferred specimen orientation in single-particle cryo-EM through tilting. *Nature Methods* **14**, 793–796.

53. Pintilie, G., Zhang, K., Su, Z., Li, S., Schmid, M.F., Chiu, W., (2020). Measurement of atom resolvability in cryo-EM maps with Q-scores. *Nature Methods* **17**, 328–334.

54. Pettersen, E.F., Goddard, T.D., Huang, C.C., Couch, G.S., Greenblatt, D.M., Meng, E.C., et al., (2004). UCSF Chimera?A visualization system for exploratory research and analysis. *J. Comput. Chem.* **25**, 1605–1612.

55. Goddard, T.D., Huang, C.C., Meng, E.C., Pettersen, E.F., Couch, G.S., Morris, J.H., et al., (2018). UCSF ChimeraX: meeting modern challenges in visualization and analysis. *Protein Sci.* **27**, 14–25.

56. Pettersen, E.F., Goddard, T.D., Huang, C.C., Meng, E.C., Couch, G.S., Croll, T.I., et al., (2021). UCSF ChimeraX: structure visualization for researchers, educators, and developers. *Protein Sci.* **30**, 70–82.

57. Sievers, F., Higgins, D.G., (2018). Clustal Omega for making accurate alignments of many protein sequences. *Protein Sci.* **27**, 135–145.

58. Waterhouse, A.M., Procter, J.B., Martin, D.M.A., Clamp, M., Barton, G.J., (2009). Jalview Version 2—a multiple sequence alignment editor and analysis workbench. *Bioinformatics* **25**, 1189–1191.